

Terahertz dark-field imaging of biomedical tissue

T. Löffler, T. Bauer, K. J. Siebert, and H. G. Roskos

Physikalisches Institut, Johann Wolfgang Goethe - Universität Frankfurt, Robert-Mayer-Straße 2-4, D-60054 Frankfurt (Main), Germany <http://www.rz.uni-frankfurt.de/piweb/femto/index.html>

A. Fitzgerald

Centre of Medical Imaging Research, University of Leeds, Great George Street, Leeds LS1 3EX, England

S. Czasch

Institut für Veterinär-Pathologie, Universität Gießen, Frankfurter Str. 96, D-35392 Gießen, Germany

Abstract: We investigate dark-field imaging in the terahertz (THz) frequency regime with the intention to enhance image contrast through the analysis of scattering and diffraction signatures. A gold-on-TPX test structure and an archived biomedical tissue sample are examined in conventional and dark-field transmission geometry. In particular, the capability of the technique for tumor detection is addressed.

©2001 Optical Society of America

OCIS codes: 110.3080, 260.3090, 300.6270

References and Links

1. R.M. Woodward, B. Cole, V. P. Wallace, D. D. Arnone, R. Pye, E. H. Linfield, M. Pepper, and A. G. Davies, "Terahertz pulse imaging of in-vitro basal cell carcinoma samples," CLEO, CWE4, pp. 329, (2001).
2. D. Arnone, C. Ciesla, and M. Pepper, "Terahertz imaging comes into view," Physics World, 35-40 (April 2000).
3. P. Y. Han, G. C. Cho, and X.-C. Zhang, "Time-domain transillumination of biomedical tissue with terahertz pulses," Opt. Lett. 25, 242-244 (2000).
4. K. J. Siebert, H. Quast, R. Leonhardt, T. Löffler, M. Thomson, T. Bauer, H. G. Roskos, and S. Czasch, "All optoelectronic CW-THz imaging", submitted to Appl. Phys. Lett.
5. D. M. Mittleman, G. Gupta, B. Neelamani, R. G. Baraniuk, J. V. Rudd, and M. Koch, "Recent advance in terahertz imaging", Appl. Phys. B 68, 1085-1094 (1999).
6. Z. Jiang and X.-C. Zhang, "2D measurement and spatio-temporal coupling of few-cycle THz pulses," Optics Express 5, 243-248 (1999), <http://www.opticsinfobase.org/ViewMedia.cfm?id=63438&seq=0>.
7. J. T. Darrow, X.-C. Zhang, D. H. Auston, and J. D. Morse, "Saturation Properties of Large-Aperture Potoconducting Antennas," IEEE J. Quantum Electron. 28, 1607-1616 (1992).

1. Introduction

Due to its contrast-formation potential in combination with its non-ionising character, THz radiation emerges as a novel spectroscopic and imaging tool in medical diagnostics [1-4]. Generated and detected optoelectronically as THz pulses [1-3,5,6] or continuous waves [4], the radiation is generally employed to determine the reflection [1] and transmission [2-5,6] properties of samples at single points or pixel by pixel over a larger area. The probing of surface and subcutaneous properties of skin [1] and the detection of tooth decay [2] are prominent examples of possible application areas of the technique.

In this paper, we investigate dark-field imaging, a well-established technique in the visible and near-infrared spectral range, but not studied yet in the context of optoelectronic THz imaging. Dark-field imaging deals with contrast enhancement by the detection of that part of the radiation which is deflected out of the beam-propagation direction by either diffraction or scattering in the sample, and requires blocking of the ballistic part of the radiation. As scattering and diffraction are also sensitive to sub-wavelength spatial structures, this technique may not only provide image contrast improvements but also give information on spatial features beyond the resolution of bright-field imaging.

2. Experimental setup

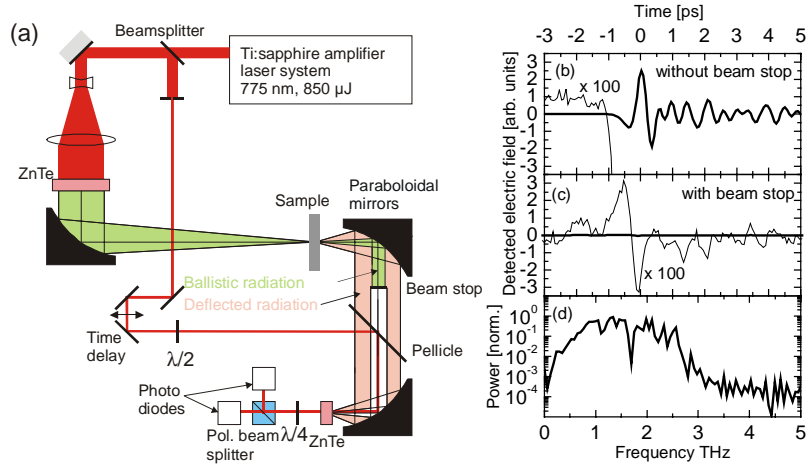


Fig. 1. (a) Experimental setup. Detected electric field without (b) and with (c) the beam stop placed into the beam. The thin lines show the signal enlarged by a factor of 100. (d) Power spectrum of the signal in (b). Absorption of water vapour is visible.

The experimental setup is outlined in Fig. 1(a). A Clark CPA 2001 amplifier laser system supplies laser pulses with 150-fs duration at 775 nm with a repetition rate of 1 kHz. The THz pulses are generated via optical rectification [2,3,6] in a $\langle 110 \rangle$ -ZnTe crystal with an area of 3 cm^2 and a thickness of $500 \text{ }\mu\text{m}$ using optical pulses with an energy of $300 \text{ }\mu\text{J}$. The THz radiation is focused onto the sample by a paraboloidal mirror with 120-mm off-axis distance producing a radiation cone with a full angle of 10° . The radiation is then collected by a second paraboloid with 50-mm off-axis distance and focused onto the detector crystal by another paraboloidal mirror (off-axis distance 40 mm). The second and third paraboloid have an effective aperture with a diameter of 40 mm, which allows the collection of radiation coming from the sample within a cone angle of 45° . As the solid angle of collection is much larger than the solid angle covered by the incident radiation, one can detect a large amount of radiation diffracted and scattered within the sample in addition to the ballistic radiation. In order to perform dark-field imaging, the latter is blocked by a metal beam stop of 1.5 cm diameter, placed behind the second paraboloidal mirror. The THz radiation is then detected electrooptically in a 1-mm-thick $\langle 110 \rangle$ -oriented ZnTe crystal. The optical probe beam used for detection is overlapped with the THz beam by a pellicle beam-splitter placed in front of the last focusing mirror.

Figure 1 shows typical THz waveforms obtained without a sample in the beam path. Figures 1(b) and (c) display typical THz waveforms detected without and with the beam stop in place, respectively. Each data set represents a single time scan with the time constant of the lock-in amplifier set to 30 ms. Without the beam stop, a peak signal-to-noise ratio of 1000:1 is achieved in the time domain. The spectrum of the signal (see Fig. 1(d)) indicates a useful frequency range from 0.3 to at least 2.5 THz. With the beam stop in place, 99 % of the ballistic signal is blocked.

3. Test structures

In order to characterise the system we performed measurements on two test structures. Both of these samples consist of a thin gold-film pattern fabricated on a TPX (Methylpentene Copolymer, Mitsui Chemicals) substrate by optical lithography. TPX is highly transparent at the relevant THz frequencies and does not show a noticeable scattering signal. The first structure is a straight-edge boundary between a metallised and a non-metallised region. An area of $6 \text{ mm} \times 2 \text{ mm}$ across the edge was scanned with a pixel spacing of 0.25 mm in both

directions. At each pixel position, a single time scan over 3.2 ps and with 100-fs delay steps was performed. The total measurement time was 0.5 hours. The following figures display the THz power transmittance relative to the transmittance of pure TPX for various frequencies. The spectral data at each pixel were obtained by Fourier transformation of the respective time-domain traces.

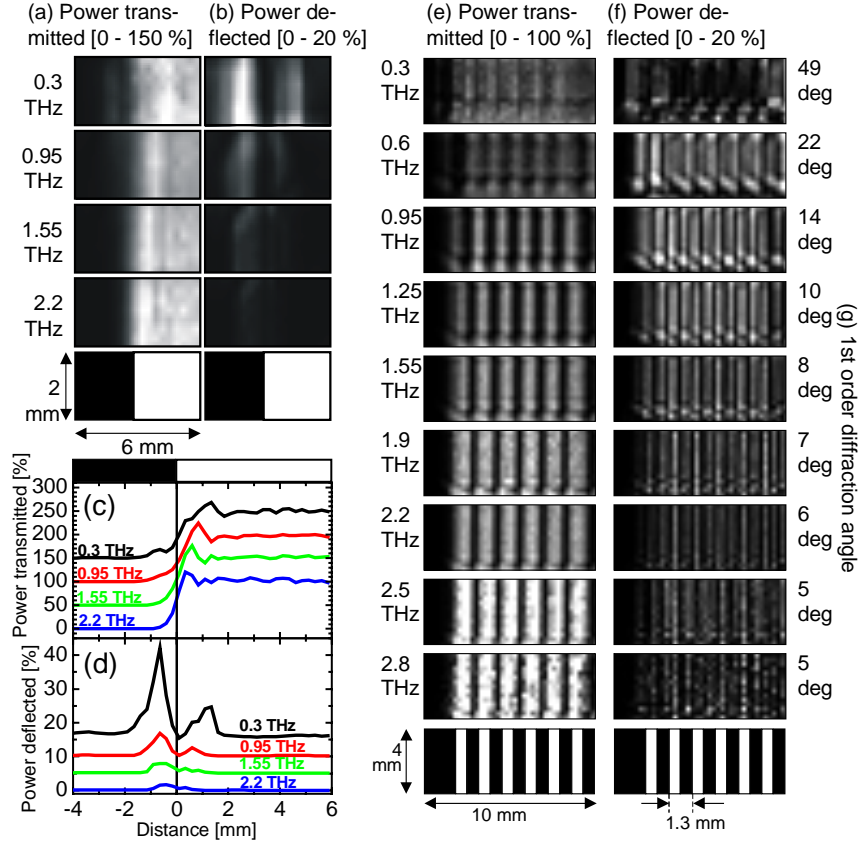


Fig. 2. THz power-transmittance (a) and deflected-power (b) images of the edge test structure for various frequencies. In the bottom panels the location of the gold (black region) and TPX (white region) are indicated. (c) and (d): the corresponding line functions (the curves are shifted for visibility). THz power transmittance of the grid test structure (e) and detected dark-field signal (f) for various frequencies. In the bottom panels the layout of the grid test structure is indicated. Additionally, the calculated angle for the first-order diffraction pattern is listed (g).

Figure 2(a) displays power-transmittance images for frequencies from 0.3 THz to 2.2 THz, Fig. 2(c) shows the corresponding line scans. The panel at the bottom of Fig. 2(a) exhibits the geometrical shape of the imaged pattern. Both the THz image and the line scan do not reproduce the actual abruptness of the edge but rather consist of broad and modulated features, due to the finite THz beam spot size and diffraction effects. The modulations are formed by interference of the transmitted electric field with the field diffracted at the edge into the detector. The overshoot of the signal amplitude to values above 100% is an aperture effect at the detector; the THz focus which is larger than the active detector area is deformed in a way the electric field at the active area is enlarged by constructive interference with the diffracted radiation. With rising frequency the image features scale in towards the edge due to the reduction of the beam diameter in the focus.

Figures 2(b) and (d) exhibit corresponding data of a dark-field measurement (with the beam stop placed in the beam). The dark-field signal consists of two asymmetric peaks; the

dominant peak on the left corresponding to the position where most of the THz beam is blocked. The signal strength decreases significantly with frequency, and the peaks are located closer to the edge region. The peaks in this case are formed by diffracted (and some scattered) radiation alone; the ballistically transmitted radiation is filtered out. We attribute the strong increase of the dark-field signal at lower frequencies to the larger skin depth in the Au metallisation, such that a larger area of the metal can contribute to the diffracted signal. In addition the deflection of THz radiation away from the ballistic path is stronger at lower frequencies, hence, more diffracted radiation is collected in the dark-field cone. The more pronounced localization of the peaks closer to the edge at higher frequency is again a result of the reduced focus diameter. We end the discussion of the edge test structure by pointing out that isolating the diffracted signal with the beam stop leads indeed to an enhancement of the edge contrast in THz imaging (best seen in the line scans of Fig 2(d)).

The second test structure is a grid of 0.65-mm-wide metal stripes with a grid constant of 1.3 mm as indicated in the bottom panels of Fig. 2(e,f). An area of 10 mm \times 4 mm was scanned with the previous parameters within a total measurement time of 1.5 hours. In Fig. 2(e), the relative THz power transmittance is depicted for various frequencies. With rising frequency, the brightness increases and the contrast is significantly improved. Both result from a reduction of the focal diameter in the beam waist with the reduced wavelength.

Figure 2(f) displays corresponding dark-field data. The most striking feature for all but the lowest two frequencies is the line doubling in the THz image which results from the fact that both edges of each gold stripe produce a diffraction signal. At low frequencies, diffraction is similar to that of a double slit because the radius of the beam waist is large enough to cover two slits. At higher frequencies, at and above 1 THz, only a single slit is illuminated and at the highest frequencies, diffraction becomes similar to that of the single edge, which has been described above. The highest brightness is found in the images taken at 0.6 THz, 0.95 THz and 1.25 THz because there, diffraction is strong and in contrast to 0.3 THz, the deflected radiation falls within the detection cone, which has an angular capture range between 15° and 45°. For illustration, Fig. 2(g) lists the angle of the first-order diffraction maximum for each frequency assuming double-slit diffraction. At 0.3 THz, the maximum lies outside of the detection cone, but falls into it at higher frequencies. The decrease of the dark-field signal observed at high frequencies is a consequence of the decrease of the diffraction efficiency.

4. Biomedical tissue

In order to investigate biomedical applications of the technique, we performed measurements on a canine skin tissue sample containing a mast cell tumour. The tissue is formalin fixed, alcohol dehydrated and embedded in paraffin wax. The sample is 3 mm thick and an area of 16 mm \times 34 mm was imaged with a pixel spacing of 0.5 mm. Figure 3(a) (bottom left) exhibits an optical image of the scanned area of the sample. Areas of fat, skin with hairs, connective tissue and the tumour are indicated. The crack in the middle of the sample results from a cut into the sample during the preparation process. At each pixel, a time scan over 6.4 ps was performed with a delay step of 100 fs. The total measurement time was 3 hours.

Images of the total loss (one minus the ratio of the power transmitted relative to the power transmitted through pure paraffin) obtained from a measurement without beam stop are depicted in Fig. 3(b) for 0.6 THz and in Fig. 3(c) for 2 THz. The contrast in the images results mainly from absorption and deflection of radiation out of the detection cone; reflection changes, on the other hand, are negligible because the refractive index varies only between 1.4 and 1.7 across the sample (deduced from the phase information of the THz transients). The data indicate that the total losses significantly increase with frequency. A particularly high total loss is observed at the boundaries between different types of tissue and in the region of the skin with hairs, and to a lesser degree in the tumour regions. It is also pointed out that a dynamic range of five orders of magnitude is achieved at the given frequencies.

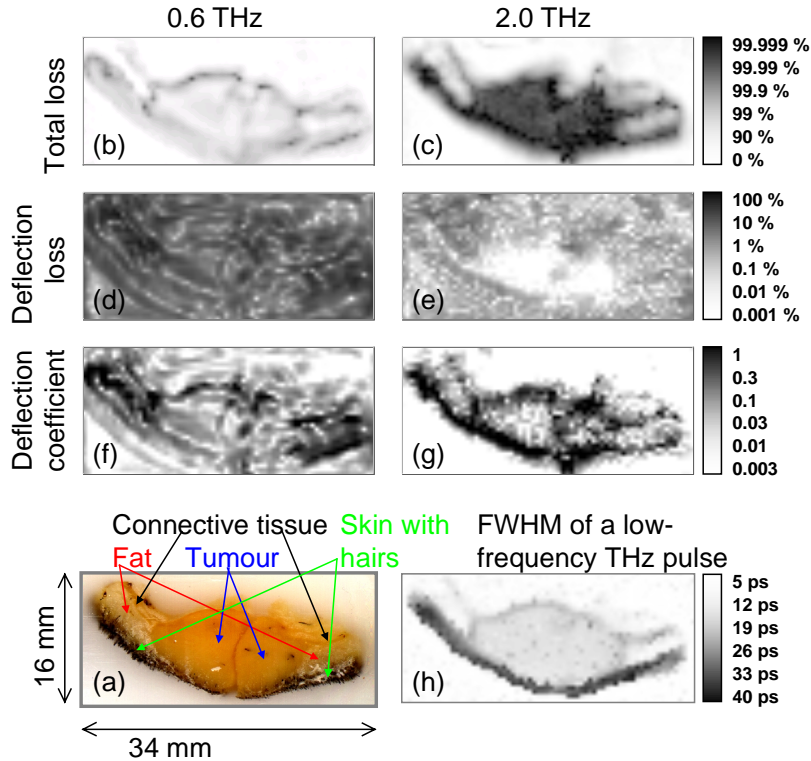


Fig. 3. (a) Optical image of the sample; (b) and (c): Total loss in transmission, (d) and (e): Loss induced by deflection; (f) and (g): Deflection coefficient. (h) Pulse duration (FWHM) of a low-frequency THz pulse. Click on Fig. 3 to see the data as a function of the frequency. (1.5 MB QuickTime movie)

The second measurement was performed with the beam stop in place, hence only signal components deflected, either by scattering or diffraction, were detected. The images in Figs. 4(d) and (e) display the deflection loss (the ratio of the power deflected relative to the power transmitted through pure paraffin) for 0.6 THz and 2.0 THz. The loss decreases with increasing frequency. In the tumor region, the loss at 2.0 THz is exceedingly small (in fact, the measured THz signal is of the order of the noise level). At the same time, the total loss (see Fig. 3(c)) is high. This can only be explained by strong absorption in the tumor region. Unfortunately, the deflection loss is not only determined by the deflection capability but also by the finite transmittance of the sample. In order to compensate for the latter, we define a new quantity; the deflection coefficient, as the ratio of the deflection loss to the absorption loss. This quantity is equivalent to the relative part of the power that would be deflected from a non-absorbing or infinitely thin sample. The resulting images are depicted in Figs. 3(f) and (g). The data taken at 2.0 THz show that the tumour region is not a strong deflector quite in contrast to the boundaries between different tissue types and the area of the skin with hairs. Comparison with the data taken at 0.6 THz suggests that diffraction is dominant at boundaries (see interference-like signal pattern at 0.6 THz), while scattering dominates in the region of skin with hairs (see weaker signal in the 0.6 THz image, consistent with reduced Rayleigh scattering at lower frequency).

In an earlier experiment, we took a standard transmission image with a THz-imaging system employing a biased GaAs large-area antenna as THz emitter [7] which has a longer pulse duration than the ZnTe emitter. The image shown in Fig. 3(h) displays the pulse duration (FWHM) of the transmitted THz signals. The pulse duration increases at the boundaries between different tissue types and even more so within the area of skin with hairs.

An analysis of the amplitude and phase data indicates that the increase of the pulse duration mainly results from a loss of high-frequency pulse components and not from dispersion. There is a remarkable similarity between Figs. 3(g) and (h), which suggests that pulse-duration images for this type of samples contain information related to that of the corresponding dark-field images.

5. Tissue recognition

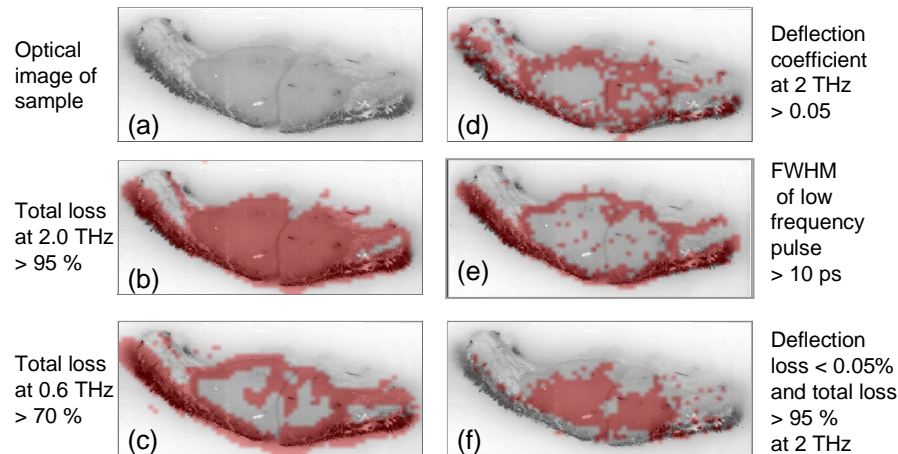


Fig. 4. Optical image of the sample (a) overlapped in (b) – (f) with a red mask generated by applying a threshold on various parameters derived from the THz data.

We now address the applicability of the various imaging techniques for tissue recognition. For this purpose, we overlay an optical grey-scale image of the sample (Fig. 4(a)) with red masks representing the portion of the sample images which fulfil the indicated threshold conditions stated in Figs. 4(b)–4(f). For example, Fig. 4(b) shows that the total loss at 2.0 THz highlights the strongly absorbing tumor tissue, the highly deflecting skin with hairs and the connective tissue areas. At 0.6 THz, the total-loss parameter enables detection of the tissue boundaries, where diffraction losses dominate, and the regions of skin with hairs, where scattering occurs (Fig. 4(c)). These areas can also be identified by inspecting the deflection coefficient at 2.0 THz (Fig. 4(d)) or the pulse duration (Fig. 4(e)). Fig. 4(f) demonstrates that the tumor region may be identified by combining criteria for the total loss and the deflection loss at 2 THz.

6. Summary and outlook

We have investigated THz dark-field imaging as a technique to discriminate between scattering/diffraction losses and absorption losses and to enhance image contrast at boundaries and edges. We have demonstrated with an archived canine skin tissue sample that the technique may be employed for tumor identification. It remains to be seen whether identification can be done routinely and reliably with varying samples. Given the fact that the clinical distinction between benign and malignant tumours is usually based on differences in the structure of the boundary between tumour and healthy tissue, dark-field imaging techniques hold much promise to be especially sensitive to these morphological differences. In this context, THz dark-field imaging must be tested in the future for its applicability for tumor detection in fresh, i.e., non-dehydrated tissue. Reflective techniques must be explored because of the strong absorption of THz radiation in water.

This work was supported by EU project TERA-VISION under contract no. IST-1999-10154 and by GSI contract no. OF-ROS.